

A novel multifrequency technique for the detection of point sources in cosmic microwave background maps

D. Herranz,^{1★} M. López-Caniego,² J. L. Sanz^{1,3} and J. González-Nuevo⁴

¹*Instituto de Física de Cantabria, CSIC-UC, Av los Castros s/n, Santander, 39005, Spain*

²*Astrophysics Group, Cavendish Laboratory, J.J. Thomson Avenue, Cambridge CB9 0E1*

³*CNR Istituto di Scienza e Tecnologie dell'Informazione, via G. Moruzzi 1, I-56124, Pisa, Italy*

⁴*SISSA-I.S.A.S., via Beirut 4, I-34014, Trieste, Italy*

Accepted 2008 December 4. Received 2008 October 28; in original form 2008 August 3

ABSTRACT

In this work we address the problem of simultaneous multifrequency detection of extragalactic point sources in the maps of the cosmic microwave background. We apply a new linear filtering technique, the ‘matched matrix filters’, that incorporates full spatial information, including the cross-correlation among channels, without making any a priori assumption about the spectral behaviour of the sources. A substantial reduction of the background is achieved thanks to the optimal combination of filtered maps. We describe the new technique in detail and apply it to the detection of radio sources and estimation of their parameters in realistic all-sky *Planck* simulations at 30, 44, 70 and 100 GHz. Then, we compare the results with the single-frequency approach based on the standard matched filter, in terms of reliability, completeness and flux accuracy of the resulting point source catalogues. The new filters outperform the standard matched filters for all these indexes at 30, 44 and 70 GHz, whereas at 100 GHz both kinds of filters have a similar performance. We find a notable increment of the number of true detections for a fixed reliability level. In particular, for a 95 per cent reliability we practically double the number of detections at 30, 44 and 70 GHz.

Key words: methods: data analysis – techniques: image processing – surveys – cosmic microwave background – radio continuum: galaxies.

1 INTRODUCTION

From the search of extrasolar planets to the study of active galactic nuclei, one of the most common tasks in all the branches of astronomy is the detection of faint point-like objects. Such objects have angular sizes that are smaller than the angular resolution of the telescopes that are used to observe them, and therefore they are usually referred to as *point sources*.

A case of particular interest is the detection of extragalactic point sources (EPS) in maps of the cosmic microwave background (CMB). EPS are known to be a relevant source of contamination for CMB studies, especially at small angular scales, where they hamper the estimation of CMB angular power spectrum both in temperature (Toffolatti et al. 1998; de Zotti et al. 1999; Hobson et al. 1999; de Zotti et al. 2005) and in polarization (Tucci et al. 2004, 2005). Therefore, for the sake of CMB analysis it is necessary to detect and remove as many EPS as possible.

Moreover, in the frequency range spanned by CMB experiments the properties of EPS are poorly studied. Only very recently the

Wilkinson Microwave Anisotropy Probe (WMAP) satellite (Bennett et al. 2003) has permitted the obtaining of the first all-sky complete point source catalogues above ~ 0.8 –1 Jy in the 23–94 GHz range of frequencies (Bennett et al. 2003; Chen & Wright 2008; Hinshaw et al. 2007; López-Caniego et al. 2007; Wright et al. 2008). The upcoming *Planck* mission (Tauber 2005) will allow us to extend these catalogues down to lower flux limits and up to 857 GHz. There are interesting physics to be probed in this frequency range. The new EPS catalogues provided by next generation CMB experiments will not only allow us to follow the behaviour of source counts from existing catalogues to microwave frequencies, but also allow us to study source variability and to discover rare objects, such as inverted spectrum radio sources, extreme gigahertz-peaked spectrum (GPS) sources and high-redshift dusty galaxies [see e.g. the *Planck Bluebook* (The Planck Collaboration 2006) for a brief, yet comprehensive review of the rich phenomenology of EPS at microwave frequencies]. Thus, the task of detecting point sources is important not only from the point of view of CMB science but also from the point of view of extragalactic astronomy.

Let us consider a single image taken at a given wavelength. Then, the problem consists of how to detect a number of objects, all of them with a common waveform that is generally considered to be well

★E-mail: herranz@ifca.unican.es

known (basically, the shape of point sources is that of the beam) but with unknown positions and intensities that are embedded in additive noise (not necessarily white). In the field of microwave astronomy, wavelet techniques (Vielva et al. 2001, 2003; González-Nuevo et al. 2006; Sanz et al. 2006; López-Caniego et al. 2007), matched filters (MFs; Tegmark & de Oliveira-Costa 1998; Barreiro et al. 2003; López-Caniego et al. 2006) and other related linear filtering techniques (Sanz, Herranz & Martínez-González 2001; Chiang et al. 2002; Herranz et al. 2002a,b; López-Caniego et al. 2004, 2005a,b) have proved to be useful. The common feature of all these techniques is that they rely on the prior knowledge that the sources have a distinctive spatial behaviour (i.e. a known spatial profile, plus the fact that they appear as compact objects as opposed to ‘diffuse’ random fields) that helps to distinguish them from the noise. Detection can be further improved by including prior information about the sources, i.e. some knowledge about their intensity distribution, in the frame of a Bayesian formalism (Hobson & McLachlan 2003; Carvalho, Rocha & Hobson 2008).

Most of the current and planned CMB experiments are able to observe the sky at several wavelengths simultaneously. Multiwavelength information makes it possible to separate different astrophysical components (e.g. CMB from the Galactic synchrotron emission) that have different spectral behaviour. Although multiwavelength component separation techniques have been very successful in separating diffuse components (for a recent comparative review of several methods applied to sky simulations very similar to the ones we will use in this paper see Leach et al. 2008), the detection of EPS has been usually attempted on a channel-by-channel basis. The reason for this is that EPS form a very heterogeneous population, constituted by a large number of objects with very different physical properties, and therefore it is impossible to define a common spectral behaviour for all of them. The whole situation remains somewhat unsatisfactory: on the one hand, the channel-by-channel approach based on the spatial behaviour works fine, but a valuable fraction of the information that multiwavelength experiments can offer is wasted this way. On the other hand, standard component separation techniques based on spectral diversity have problems when dealing with the very heterogeneous EPS components.

Thus, multiwavelength detection of EPS in CMB images remains a largely unexplored field. In recent years, some attempts have been made in this direction. For example, Naselsky, Novikov & Silk (2002) combined simulated multiwavelength maps in order to increase the average signal-to-noise ratio of point sources. In a similar way, Chen & Wright (2008) and Wright et al. (2008) used combinations of the *WMAP* *W* and *V* bands in order to produce a CMB-free map to better detect the elusive radio galaxies. Note that, in any case, combined ‘clean’ maps are suitable for detecting more sources but not for performing accurate photometry, unless the spectral index of all the sources is known in advance.

An intermediate approach is to design filters that are able to find compact sources thanks to their distinctive spatial behaviour while at the same time do incorporate some multiwavelength information, without pretending to achieve a full component separation and without assuming a specific spectral behaviour for the sources. Very recently, the authors have proposed a new technique, based on the ‘matched matrix filters’ (MTXF; Herranz & Sanz 2008), that goes in this direction. The basic underlying ideas of the new method are as following.

(i) When a source is found in one channel, it will also be present in the same position in all the other channels.

(ii) The spatial profile of the sources may differ from channel to channel, but it is a priori known.

(iii) The second-order statistics of the background in which the sources are embedded are well known or it can be directly estimated from the data by assuming that point sources are sparse. This knowledge about the second-order statistics (namely, the background’s power spectrum for each channel and the its correlations among the different channels) will be used to increase the signal-to-noise ratio of the sources.

(iv) We want to perform an accurate photometry of the sources at each one of the frequencies covered by the experiment, independently of what is the spectral behaviour of any source in particular.

In Herranz & Sanz (2008), the authors presented the new methodology and demonstrated its potential utility with a few toy simulations. In this paper, we will study its applicability to real CMB experiments by applying it to realistic simulations of the whole sky as will be observed by the upcoming *Planck* mission. We will focus on the particular case of the detection of radio sources in the four lower frequency *Planck* channels (33–100 GHz), comparing the performance of the new filters with the performance of the well-established standard MFs. In Section 2, we will summarize the foundations of the theoretical formulation of MTXF. In Section 3, we will describe the *Planck* simulations that we use to test the method and we will outline the main features of the code we have developed for its implementation. The results of the exercise will be described in Section 4. Finally, in Section 5 we will draw some conclusions.

2 MATCHED MATRIX FILTERS

The derivation of the MTXF is fully described in Herranz & Sanz (2008).¹ However, for reasons of clarity, we will reproduce the main ideas of that paper here.

2.1 Data model

Let us consider a set of N two-dimensional images (channels) in which there is an unknown number of point sources embedded in a mixture of instrumental noise and other astrophysical components. Without loss of generality, let us consider the case of a single point source located at the origin of the coordinates. Our data model is

$$D_k(\mathbf{x}) = s_k(\mathbf{x}) + n_k(\mathbf{x}), \quad (1)$$

where the subscript $k = 1, \dots, N$ denotes the index of the image. The term $s_k(\mathbf{x})$ denotes the point source,

$$s_k(\mathbf{x}) = A_k \tau_k(\mathbf{x}), \quad (2)$$

where A_k is the unknown amplitude of the source in the k th channel and $\tau_k(\mathbf{x})$ is the spatial profile of the source (which is assumed to be known) and satisfies the condition $\tau_k(\mathbf{0}) = 1$. The term $n_k(\mathbf{x})$ in equation (1) is the generalized noise in the k th channel, containing not only instrumental noise, but also CMB and all the other astrophysical components apart from the point sources. Let us suppose that the noise term can be characterized by its cross-power spectrum:

$$\langle n_k(\mathbf{q}) n_l^*(\mathbf{q}') \rangle = P_{kl}(\mathbf{q}) \delta^2(\mathbf{q} - \mathbf{q}'), \quad (3)$$

¹ For economy, in the following we will occasionally refer to the MTXF just as ‘matrix filters’.

where $\mathbf{P} = (P_{kl})$ is the cross-power spectrum matrix and the symbol ‘*’ denotes complex conjugation. From now on, we assume that the noise has zero mean:

$$\langle n_k(\mathbf{x}) \rangle = 0. \quad (4)$$

2.2 Filtering with matrices of filters

Since we are interested in doing accurate photometry in each one of the N available channels, we are bound to produce N different processed maps. Therefore, we are looking for a transformation that starts with N input channels and ends with other N processed maps, where (i) point sources are easier to detect and (ii) the amplitudes A_k are preserved. Besides, since we intend to use some multiwavelength information, we are interested in making all the N input channels intervene in the elaboration of all the output maps. One possibility is to define a set of $N \times N$ filters $\Psi_{kl}(\mathbf{x})$ such that the N combined quantities

$$\begin{aligned} w_k(\mathbf{x}) &= \sum_l \int d\mathbf{x}' \Psi_{kl}(\mathbf{x} - \mathbf{x}') D_l(\mathbf{x}') \\ &= \sum_l \int d\mathbf{q} e^{-i\mathbf{q} \cdot \mathbf{x}} \Psi_{kl}(\mathbf{q}) D_l(\mathbf{q}) \end{aligned} \quad (5)$$

are our processed maps. The last term of the equation is just the expression of the filterings in Fourier space, being \mathbf{q} the Fourier mode and $\Psi_{lk}(\mathbf{q})$ and $D_l(\mathbf{q})$ the Fourier transforms of $\Psi_{kl}(\mathbf{x})$ and $D_l(\mathbf{x})$, respectively.

We intend to use the combined filtered image $w_k(\mathbf{x})$ as an estimator of the source amplitudes A_k for all $k = 1, \dots, N$. Thus, the filters Ψ_{kl} must satisfy the condition that the k th filtered, combined image at the position of the source is, on average over many realizations, an *unbiased* estimator of the amplitude of the k th source. The other requirement we will ask the processed maps is that the signal-to-noise ratio of the sources is increased with respect to the input maps. In other words, we want estimators w_k to be not only unbiased, but *efficient* as well. Therefore, we need to minimize the variance σ_{w_k} of the combined filtered image.

The set of filters that minimizes the variance σ_{w_k} for all k while keeping the individual amplitudes A_k constant for all the point sources, independent of their frequency dependence, can be shown to be given by the matrix equation:

$$\Psi^* = \mathbf{F} \mathbf{P}^{-1}, \quad (6)$$

where

$$\mathbf{F} = (F_{kl}), \quad \mathbf{P} = (P_{kl}), \quad \lambda = (\lambda_{kl}), \quad \mathbf{H} = (H_{kl}), \quad (7)$$

where

$$\begin{aligned} F_{kl} &= \lambda_{kl} \tau_l, \\ \lambda &= \mathbf{H}^{-1}, \\ H_{kl} &= \int d\mathbf{q} \tau_k(\mathbf{q}) P_{kl}^{-1} \tau_l(\mathbf{q}). \end{aligned} \quad (8)$$

The set of filters that we have developed naturally assumes a structure that is best expressed in the form of a matrix equation, hence the denomination of ‘*MTXF*’.

2.3 Properties of matched matrix filters and some particular cases

2.3.1 A single image

If the number of images is $N = 1$, it is easy to show that the matrix of filters contains a single element, which is the complex conjugate of the standard MF. For circularly symmetric source profiles, the filter is real-valued and the resulting filter is exactly the same as the standard MF.

2.3.2 Uncorrelated noise

From equations (6) and (8), it is straightforward to show that for the particular case where the noise is totally uncorrelated among channels the matrix of filters defaults to a diagonal matrix whose non-zero elements are the complex conjugates of the standard MFs that correspond to each input channel. When the source profiles are circularly symmetric, the filters are real-valued and the whole process is equivalent to filter each channel independently with the appropriate MF.

2.3.3 The 2×2 case

In this case, the explicit form of the MTXF is

$$\begin{aligned} \Psi_{11}^* &= \frac{1}{N\Delta} \left[\phi_1 - \phi_2 \frac{P_{12}b_{12}}{P_{11}b_{22}} \right], \\ \Psi_{12}^* &= \frac{1}{N\Delta} \left[-\phi_1 \frac{P_{12}}{P_{22}} + \phi_2 \frac{b_{12}}{b_{11}} \right], \\ \Psi_{22}^* &= \frac{1}{N\Delta} \left[\phi_2 - \phi_1 \frac{P_{12}b_{12}}{P_{22}b_{11}} \right], \\ \Psi_{21}^* &= \frac{1}{N\Delta} \left[\phi_1 \frac{b_{12}}{b_{22}} - \phi_2 \frac{P_{12}}{P_{11}} \right], \\ N &\equiv 1 - \frac{b_{12}^2}{b_{11}b_{22}}, \\ \Delta &\equiv 1 - \frac{P_{12}^2}{P_{11}P_{22}}, \\ b_{ij} &\equiv \int d\mathbf{q} \frac{\tau_i \tau_j^*}{\Delta} \frac{P_{ij}}{P_{ii}P_{jj}}, \end{aligned} \quad (9)$$

where $i, j = 1, 2$; and ϕ_i are closely related to the standard MFs ϕ_i^{MF} :

$$\begin{aligned} \phi_1 &= \frac{\tau_1}{b_{11}P_{11}} = \frac{c_1}{b_{11}} \phi_1^{\text{MF}}, \quad c_1 \equiv \int d\mathbf{q} \frac{\tau_1^2}{P_{11}}, \\ \phi_2 &= \frac{\tau_2}{b_{22}P_{22}} = \frac{c_2}{b_{22}} \phi_2^{\text{MF}}, \quad c_2 \equiv \int d\mathbf{q} \frac{\tau_2^2}{P_{22}}. \end{aligned} \quad (10)$$

We remark that the MTXF are non-symmetric matrices in general. The variances of the two filtered maps are

$$\begin{aligned} \sigma_{w_1}^2 &= \frac{1}{Nb_{11}}, \\ \sigma_{w_2}^2 &= \frac{1}{Nb_{22}}. \end{aligned} \quad (11)$$

From the last equation, one obtains

$$\frac{\sigma_{w_1}^2}{\sigma_{w_2}^2} = \frac{b_{22}}{b_{11}}. \quad (12)$$

2.3.4 Relative gain of the different channels

A useful quantity that can be used to assess the performance of a filter is its *gain* factor, i.e. the increment of the signal-to-noise ratio that is obtained thanks to the application of a filter. Of course, gain is not a universal quantity of the filter, since it depends on the statistical properties of the background noise, but given a particular image, the relative gain of two filters provides a good intuitive measurement of their respective performances. For unbiased filters (i.e. filters that preserve the amplitude of the signal), the gain is just the ratio of noise dispersions before and after filtering:

$$G = \frac{\sigma}{\sigma_w}, \quad (13)$$

where σ is the noise dispersion before filtering and σ_w is the noise dispersion after filtering.

When comparing the performances of MTXF with those of standard MFs, Herranz & Sanz (2008) observed an apparent trend: in all the few cases they studied, the gain factor of the matrix filters was similar to the one of MFs for at least one of the channels, and significantly higher for the others. Moreover, the channel with the lower gain was the one with the worse signal-to-noise ratio after filtering. At the moment, it was not clear if this was a universal trend of just a result obtained by chance given the low number of cases under study in that work. As we will see below, the results of this work seem to support this observed trend.

There is a qualitative argument that sheds light over this phenomenon: for the sake of simplicity, let us consider two channels and identical profiles $\tau_1 = \tau_2$. If one assumes that $P_{11} < P_{22}$, then the equations (10, 11) lead to

$$\sigma_{w_1} < \sigma_{w_2} \text{ and } \sigma_{w_1}^{\text{MF}} < \sigma_{w_2}^{\text{MF}} \quad (14)$$

for the MTXF and standard MF, respectively. Therefore, the original map with less variance gains more with either filter. On the other hand, assuming that $P_{12} \ll P_{11} < P_{22}$, taking into account equations (10, 11) and the Schwartz inequality, one obtains

$$\sigma_{w_i} \leq \sigma_{w_i}^{\text{MF}}, \quad (15)$$

i.e. the MTXF outperform the standard MF.

3 APPLICATION TO PLANCK RADIO SOURCES

In this section, we will describe an application of the new multi-wavelength filtering technique for realistic simulations of the sky as it will be observed by the *Planck* mission. As an example, we will focus on the blind detection of extragalactic radio sources. Therefore, we will simulate the 30, 44, 70 and 100 GHz *Planck* channels. Note that although a simultaneous multiwavelength filtering of the nine *Planck* channels is relatively easy to do (it would imply the use of a 9×9 matrix of filters that can be easily handled by any desktop computer), the addition of infrared channels would probably help little to the detection radio sources. An intuitive reason for this is that the sources that are bright in the infrared range are not necessarily the same that dominate the radio range, and vice versa. Therefore, for this work we prefer to treat the radio sources separately. Besides, the low-dimensional 4×4 application we describe here is more adequate to illustrate the technique, allowing us to show the details of the method with a relatively small number of plots.

3.1 The simulations

Sky simulations are based on the Planck Sky Model² (PSM; Delabrouille et al., in preparation), a flexible software package developed by Planck Working Group 2 (WG2) for making predictions, simulations and constrained realizations of the microwave sky. The simulated data used here are the same as in Leach et al. (2008), where the characteristics of the simulations are explained more in detail.

The CMB sky is based on a Gaussian realization assuming the WMAP best-fit C_ℓ at higher multipoles.

The Galactic emission is described by a three-component model of the interstellar medium comprising free-free, synchrotron and dust emissions. The free-free emission is based on the model of Dickinson, Davies & Davis (2003) assuming an electronic temperature of 7000 K. The spatial structure of the emission is estimated using a H α template corrected for dust extinction. The synchrotron emission is based on an extrapolation of the 408 MHz map of Haslam et al. (1982) from which an estimate of the free-free emission was removed. A limitation of this approach is that this synchrotron model also contains any dust anomalous emission seen by WMAP at 23 GHz. The thermal emission from interstellar dust is estimated using model 7 of Finkbeiner, Davis & Schlegel (1999).

Point sources are modelled with two main categories: radio and infrared. Simulated radio sources are based on the National Radio Astronomy Observatory Very Large Array Sky Survey (NVSS) or Sydney University Molonglo Sky Survey (SUMSS) and Green Bank 6 (GB6) or Parkes-MIT-National Radio Astronomy Observatory (PMN) catalogues. Measured fluxes at 1 and/or 4.85 GHz are extrapolated to Planck frequencies assuming a distribution in flat and steep populations. For each of these two populations, the spectral index is randomly drawn within a set of values compatible with the typical average and dispersion. Infrared sources are based on the *IRAS* catalogue and are modelled as dusty galaxies. In addition, the emission of a large number of blended infrared galaxies, not present individually in the *IRAS* catalogue, is simulated to model the far-infrared background (González-Nuevo, Toffolatti & Argüeso 2005). We also include in the model a map of thermal SZ spectral distortion from galaxy clusters, based on a cluster catalogue randomly drawn using a mass function compatible with present-day observations.

3.2 The code

In this work, we have used a code that reads in four all-sky Flexible Image Transport System (FITS) maps with Hierarchical Equal Area isoLatitude Pixelization (HEALPix) (Górski et al. 2005) resolution parameter NSIDE = 1024, one per frequency between 30 and 100 GHz. Secondly, according to some parameters given in an input file, the code uses the CPACK libraries³ to divide the sky in a sufficient number of overlapping flat patches such that 100 per cent of the sky is covered. In this pixelization scheme, we have produced 371 patches per frequency, 14.656 deg^2 and 256×256 pixel each. Then, the code proceeds to run either the MF or the MTXF algorithms on every set of four patches corresponding to the same region in the sky. Afterwards, once the optimally filtered image has been produced, the code looks for maxima in it, producing a subcatalogue of detections. Finally, a combined catalogue is produced, removing possible repetitions inside a 1 full width at half-maximum (FWHM) radius.

² http://www.apc.univ-paris7.fr/APC_CS/Recherche/Adamis/PSM/psky-en.php

³ <http://astro.ic.ac.uk/~mortlock/cpack/>

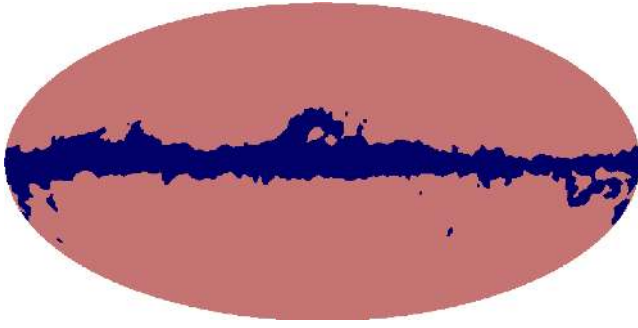


Figure 1. Mask used for the analysis. The mask covers 14.91 per cent of the sky, including the Galactic plane plus some other densely contaminated areas of the sky such as the Magellanic Clouds, the Ophiuchus Complex and the Orion/Eridanus Bubble.

4 RESULTS

As described above, we have divided the sky into square flat patches by projecting the HEALPix (Górski et al. 2005) maps into the tangent plane at a set of coordinates that are regularly distributed on the sphere. For each resulting patch we have four square images, one per frequency channel (30, 44, 70 and 100 GHz). Then, we have simultaneously filtered the four images with the filters (6) specifically calculated for that region of the sky. In parallel, we have filtered each one of the images separately with its corresponding MF. Therefore, for each input image we have two output filtered images, one obtained with the standard MF and other obtained by the matrix filters as in equation (5). Then, we have applied the same thresholding detection criterion to the two cases: for any given filtered map, we have selected all the peaks that have at least three connected pixels with flux above a given number of times the σ level⁴ of the filtered map. Unless otherwise noted, all the plots that will be shown in this section will refer to detections above the 5σ detection threshold. The detections thus obtained for the different patches have been combined into a single whole-sky catalogues for each of the four frequency channels and the two filtering schemes.

Fig. 1 shows the Galactic mask we apply for the analysis of the results. We apply the mask after filtering only to avoid the strongly contaminated regions around the Galactic plane when constructing our catalogues. The mask is similar to the *WMAP* Kp2 mask, and it covers a highly contaminated region around the Galactic plane plus a set of irregular areas that mask other highly contaminated areas of the sky such as the Magellanic Clouds, the Ophiuchus Complex and the Orion/Eridanus Bubble. In total, we are masking 14.91 per cent of the pixels of the sky.

4.1 Detail of a single patch

Before discussing the results for all the sky outside the mask just described above, let us illustrate the qualitative functioning of the filters taking as an example just one sky patch. In the first row of the plots of Fig. 4, we show the aspect of sky in the first of the patches we have studied, centred in the Galactic North Pole. It is a region of the sky with a very low contamination from Galactic emission, with two point sources that are clearly visible to the naked eye (at least at

⁴ Where σ is the standard deviation of the filtered map, excluding the region of the borders of the image; note that this σ level corresponds to a different flux threshold for different filters and regions of the sky.

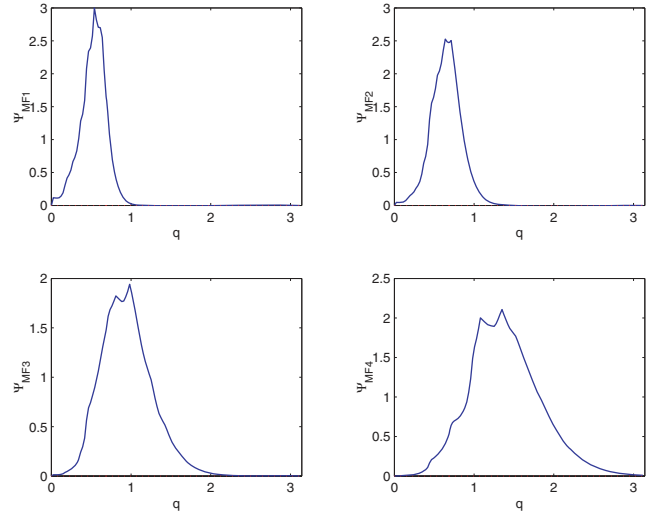


Figure 2. Standard MFs, in Fourier space, for the four channels in one of the patches considered.

30 GHz), but many others are hidden amid the diffuse components. EPS alone are shown in the second row of the plots of the figure.

Fig. 2 shows the MFs, in Fourier space, for the four different channels shown in Fig. 4. Fig. 3 shows the 16 elements of the corresponding matrix of filters, also in Fourier space. Note that the filters in the diagonal look roughly similar to the MFs whereas the off-diagonal elements are quite different. This can be intuitively explained in the following way: the diagonal element Ψ_{kk} is designed to produce a maximum contribution of the source profile τ_k in the map D_k whereas the Ψ_{kl} , $l \neq k$, element is designed to produce a minimum contribution of the source profile τ_l in the map D_k . This way the off-diagonal elements of the filtering contribute to reduce noise but do not introduce bias in the determination of the fluxes in the k th map.

The third and fourth rows of Fig. 4 show the output filtered patches for the MF and the matrix filters, respectively. Note that for the 44 and 70 GHz channels the output matrix filtered maps look far cleaner than their matched filtered equivalents. For the 30 GHz channel, the distinction is not so clear (the matrix filtered image looks cleaner, but some of the sources that are easily visible in the matched filtered image are apparently missing; we will see later that this is only a visual effect). Finally, for the 100 GHz channel both filtered images look practically identical.

The gain factors obtained for these images with the MTXF are [2.9, 3.8, 3.5, 2.8] for the [30, 44, 70, 100] GHz channels. The gain ratio between the MTXF and the MF is $G_{\text{MTXF}}/G_{\text{MF}} = [1.38, 1.52, 1.49, 1.00]$ for the [30, 44, 70, 100] GHz channels. Thus, the MTXF-filtered image with lower gain (100 GHz) is the one that is more similar to the correspondent MF-filtered image. Besides, the 100 GHz map is the one with higher variance before filtering. We will see in the next section that the all-sky results confirm this rule.

4.2 All-sky results

We can use the knowledge on the input EPS that we have simulated to control the quality of our catalogues in terms of number of true and false detections. The criterion we use to decide whether a detection is a true or a false one is purely positional: an object of the catalogue is considered a true detection if it is closer than a certain

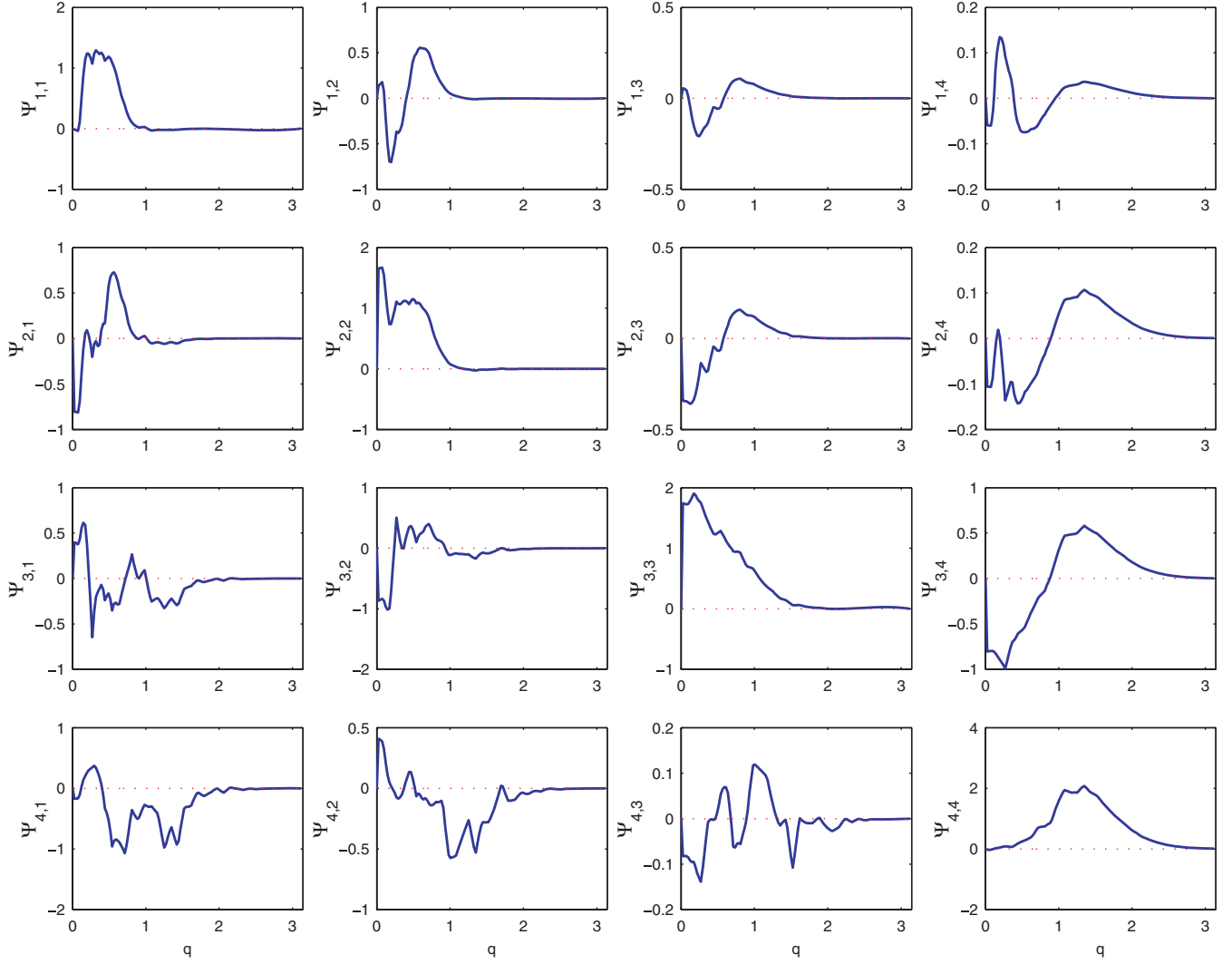


Figure 3. The different elements of the 4×4 matrix of filters, in Fourier space, for the same patches as in Fig. 2.

matching radius r of an input source and a false (spurious) detection otherwise. For this work, we use a matching radius $r = 2R_0$, where R_0 is the width of the Gaussian beam corresponding to the channel under study (namely 33.0, 24.0, 14.0 and 9.5 arcmin for the 30, 44, 70 and 100 GHz channels, respectively). This radius is smaller than 1 FWHM, so the criterion we use is quite stringent. Considerations about the flux matching will be made later in Section 4.2.5.

4.2.1 Number of detections

Fig. 5 shows the number of detected sources in our 5σ catalogues that have true fluxes $S > S_0$ as a function of the flux threshold S_0 . The number of detections obtained with the MF is shown by a solid line, whereas the number of detections obtained with the MTXF is shown by a dot-dashed line.

Two different cases can be observed: the 100 GHz channel and the other three channels. At the 100 GHz channel, the performance of the two kinds of filters is almost identical. From 30 to 70 GHz and high and intermediate fluxes (≥ 0.6 Jy), the two methods detect very similarly. The MTXF curve runs slightly below the MF curve: the difference consists of a few high-flux sources that are somehow

missed by the MTXF. We will discuss this problem in more detail below.

In the low-flux region of the plots, the number of detected sources stops growing and the curves reach a plateau. The knee point of the curves roughly indicates the detection limit of the 5σ catalogues. At 30, 44 and 70 GHz, this knee point occurs around 600 (400) mJy for the matched (matrix) filters. In other words, the MF reaches its detection limit at fluxes higher than the MTXF. Therefore, the MTXF are able to go deeper and are able to detect many more faint sources than the MF. At 100 GHz, both filters have their detection limits located around 400 mJy.

We have checked that the number of 5σ detections obtained with the MF roughly agrees (taking into account the different sky coverage) with the results obtained in previous works (López-Caniego et al. 2006; Leach et al. 2008) that have made use of similar Planck simulations.

4.2.2 Completeness

Fig. 6 shows the completeness level as a function of the flux of the 5σ catalogues obtained with the MF and the MTXF. Here, the

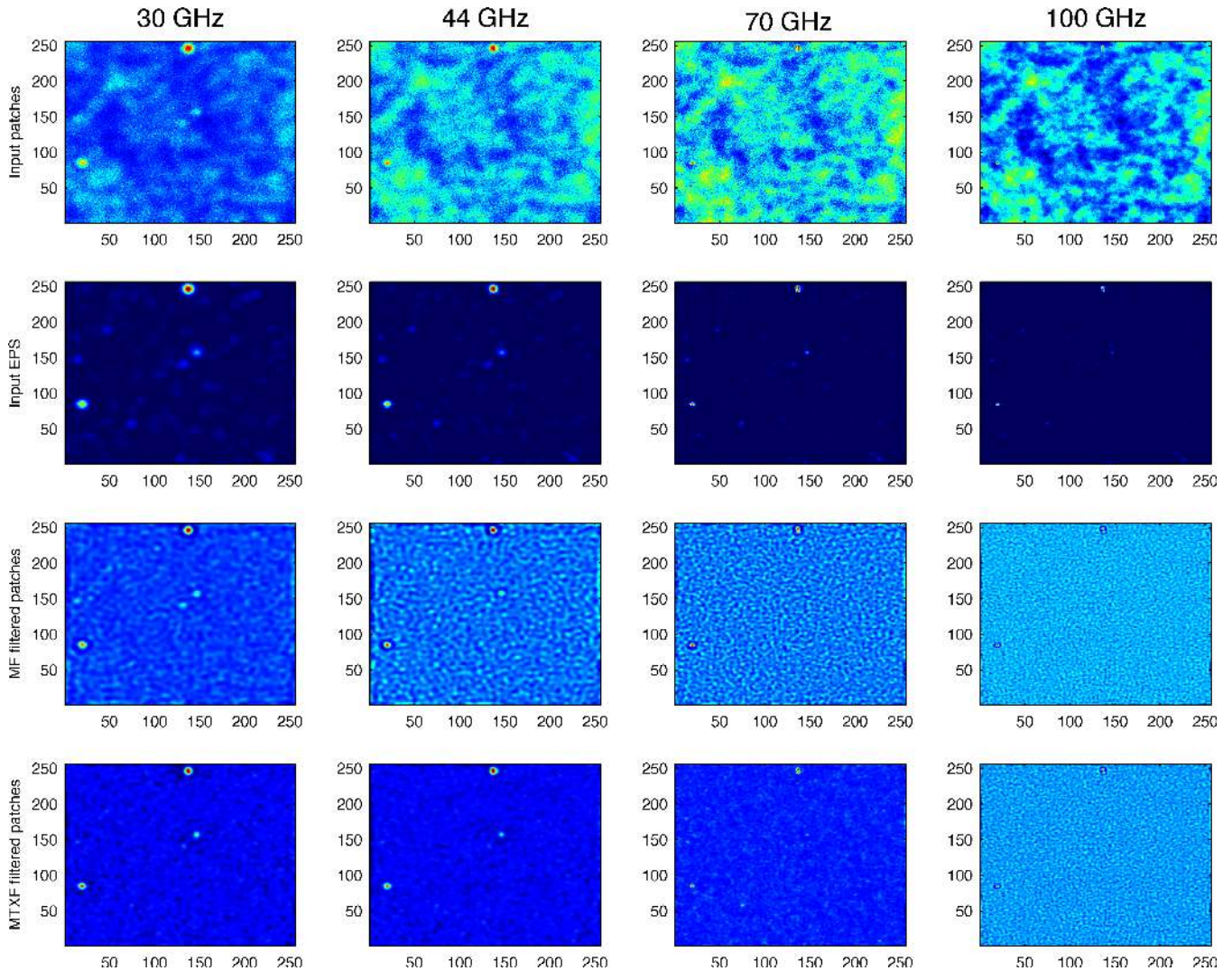


Figure 4. One of the regions of the sky. The square patch is centred in the North Galactic Pole. The first row of images, starting from the top, shows the input patches at 30, 44, 70 and 100 GHz (from left- to right-hand panels of the figure). The second row of images separately shows the EPS contribution to the input maps for the same frequencies. The third row shows the patches after having been filtered with the standard MF corresponding to each frequency. The bottom row shows the combined filtered maps resulting from the application of the matrix filters. All maps are expressed in mJy sr⁻¹ units. The x - and y -axes are in pixel units (pixel size = 3.435 arcmin).

completeness is defined, as usual, as the ratio between the number of recovered true sources and the total number of input sources over a given flux limit. The 100 and the 95 per cent completeness levels are marked by two horizontal dotted lines. The 95 per cent completeness fluxes are, for the matched (matrix) filters, the following: at 30 GHz, 610 (540) mJy; at 44 GHz, 460 (340) mJy; at 70 GHz, 390 (270) mJy and at 100 GHz, 270 (270) mJy. Three issues about Fig. 6 deserve detailed comments.

If compared to the data in table 2 of López-Caniego et al. (2006), our present completeness limits are higher than theirs. This is due to two causes: on the one hand, in this work we include regions of the sky that are closer to the Galactic plane and therefore more contaminated (and therefore, the 5σ detection threshold corresponds to a higher flux), where it is more likely to lose some sources, and, on the other hand, our present detection/selection criterion requires to have peaks with at least three connected pixels. This more stringent criterion helps to reduce the number of spurious detections, but occasionally makes us lose some true sources as well.

Regarding the different channels, for the case of 30, 44 and 70 GHz, the MTXF show a better completeness level at intermediate and low fluxes. This is because MTXF do amplify the point source signal with respect to the foregrounds better, and therefore they can reach lower detection limits. At 100 GHz, both kinds of filtering lead to the same completeness levels.

Both methods do miss some bright sources, even at fluxes > 1 Jy. For example, at 30 GHz, both the MF and the MTXF fail to detect four sources with fluxes > 1 Jy. Three of them are common for the two filters, and in all the three cases are sources that are in heavily contaminated regions at low Galactic latitude, very close to the border of the mask. Apart from these three missing sources, the MF misses a source that is detected by the MTXF, and the MTXF miss a source that is detected by the MF. The first one corresponds to a source close to the Large Magellanic Cloud and a few pixels away from our mask. The second case corresponds to a source that is 2.69 Jy source that is only 35 arcmin away from a detected 3.23 Jy source. Although the distance between both sources is

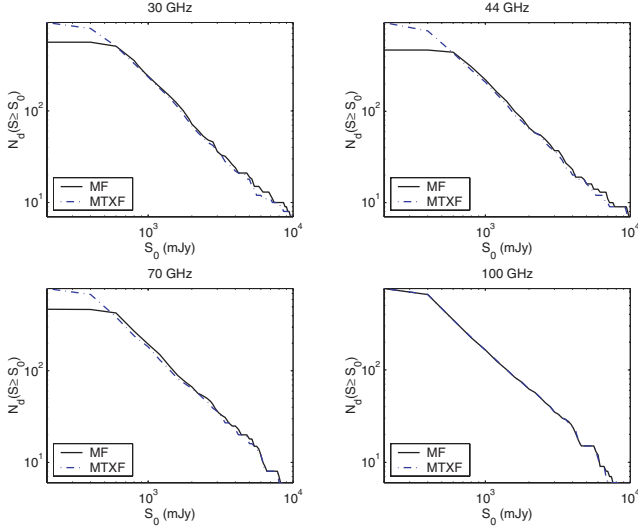


Figure 5. Number of true detections with true fluxes above a given flux value. Solid line: detections with the MF. Dot-dashed line: detections with the matrix filters.

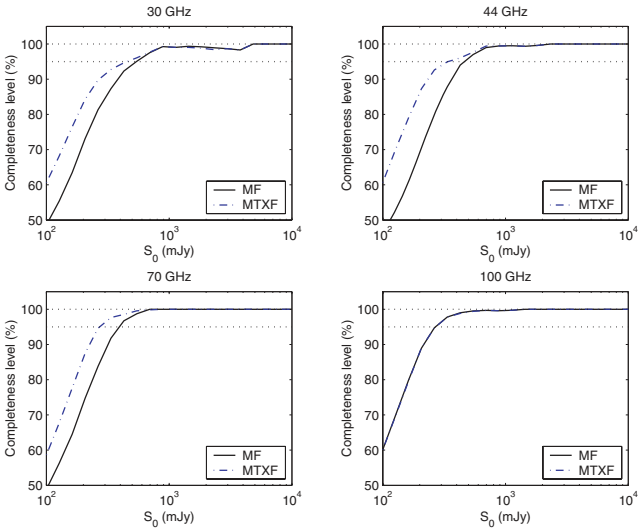


Figure 6. Completeness diagram. Solid line: MF. Dashed line: matrix filters. The 100 and the 95 per cent completeness levels are marked by two horizontal dotted lines.

slightly larger than the matching radius we used for this channel, the MTXF are unable in this case to resolve the two sources individually.

This suggests that the mask we have used is good enough to avoid most spurious detections, but it may be insufficient to guarantee completeness. Besides, a problem of blending with the MTXF arises when two high-flux sources lie very close to one another. Although this situation is not frequent, this may explain the slight loss of performance of the MTXF in Fig. 5 for high and intermediate fluxes.

4.2.3 Reliability

Another interesting indicator of the performance of the filters is the reliability of the catalogues obtained with them. Let it be $N_d(\nu)$, the number of true detections above a certain detection threshold ν , and

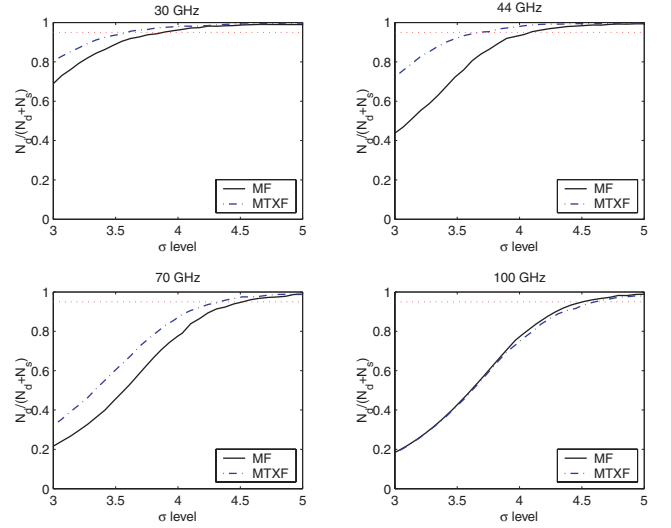


Figure 7. Reliability of the catalogues as a function of the limiting σ threshold for the two filters and the four channels. Solid line: MF. Dot-dashed line: MTXF. The dotted line shows the 95 per cent reliability level.

$N_s(\nu)$, the number of spurious detections (false alarms) above the same threshold. Then, we define the reliability in the usual way:

$$r(\nu) = \frac{N_d(\nu)}{N_d(\nu) + N_s(\nu)}. \quad (16)$$

The reliability of our 5σ catalogues is well above the 95 per cent level for the two filtering schemes and the four channels we considered. In order to show the performance of the filter for lower reliability levels, in Fig. 7 we have gone deeper in the detection, down to the 3σ level. The higher dotted line in the Fig. 7 shows the $r = 100$ per cent reliability level and the lower dotted line shows the $r = 95$ per cent reliability level. For the 30, 44 and 70 GHz channels, the MTXF allow us to go to lower detection thresholds than the MF for a fixed required reliability level. For the 100 GHz channel, the situation is the opposite, but the difference is small. Table 1 shows the threshold limits at the 95 per cent reliability level and the corresponding number of true detections for the two filters and four channels considered. The improvement of the MTXF with respect to the MF is significant for the 30, 44 and 70 GHz channels.

4.2.4 Receiver operating characteristics

Yet another way to comparatively study the performance of the two detectors is the *receiver operating characteristic* (ROC), or simply *ROC curve* (Kay 1998). ROC curves are profusely used in the detection theory because they provide a direct and natural way to relate the costs/benefits of the decision-making associated with the detection process. Let us consider the following two quantities: the *true positives ratio* (TPR) is defined as

$$\text{TPR} = \frac{N_d}{NT}, \quad (17)$$

where, as before, N_d is the number of true detections (true positives) obtained for a certain detection threshold and NT is the total number of objects (in this case, simulated point sources) in the data set. The TPR is related, but not equivalent, to the completeness defined above (the number in the denominator of the completeness depends as well on the detection threshold, but NT does not).

Table 1. Threshold $\sigma_{95 \text{ per cent}}$ limit required for a 95 per cent reliability, and corresponding number $N_{d,95 \text{ per cent}}$ of detections for such a threshold.

Frequency (GHz)	$\sigma_{95 \text{ per cent, MF}}$	$N_{d,95 \text{ per cent, MF}}$	$\sigma_{95 \text{ per cent, MTXF}}$	$N_{d,95 \text{ per cent, MTXF}}$
30	3.9	900	3.6	1600
44	4.1	705	3.7	1550
70	4.5	580	4.3	1000
100	4.5	940	4.6	895

The other quantity of interest is the spurious detection, false alarm or *false positive ratio* (FPR):

$$\text{FPR} = \frac{N_s}{FT}, \quad (18)$$

where N_s is defined as in Section 4.2.3 and FT is the total number of candidates (in our case, peaks in the filtered images) that can be identified or not as ‘detections’ (true or false) by the detector. Therefore, there is an indirect relation between FPR and the reliability, but note that the quantity in the denominator in equation (18) does not depend on the threshold. Both quantities, TPR and FPR, take values in the interval $[0, 1]$, and they are called as the *operating characteristics* of the detector. The TPR can be directly associated with the power of the detector and the FPR is related to its significance.

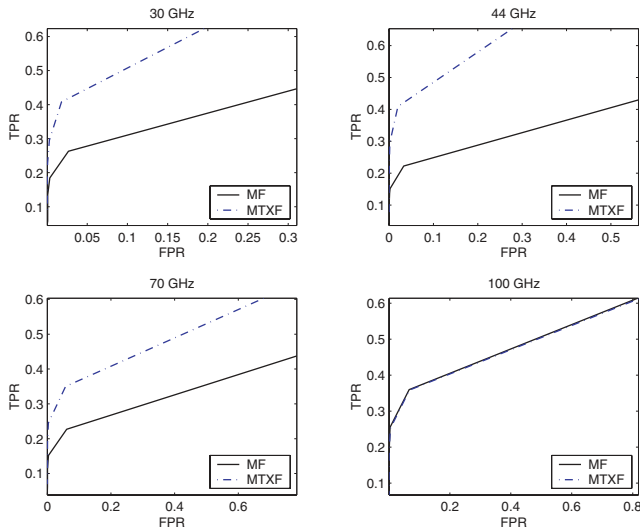
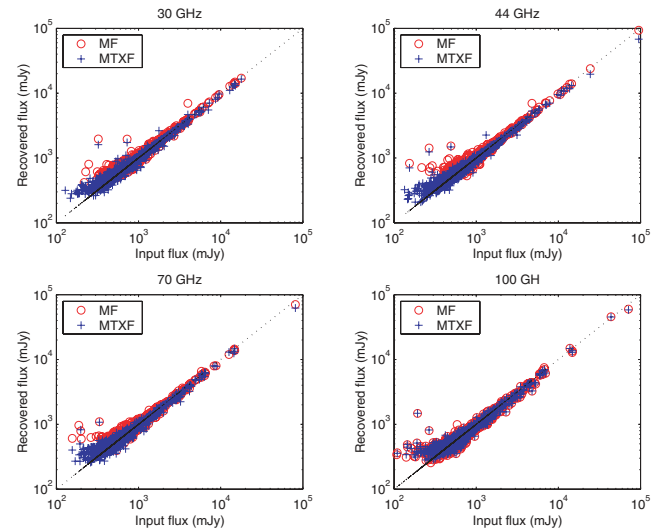
ROC curves are constructed by plotting the fraction of true positives (TPR) versus the fraction of false alarms (FPR). They convey at a single glance the same information that can be found by taking together the Fig. 7 plus a set of tables akin to Table 1 obtained at different reliability levels. For any fixed false alarm ratio, the ROC curve tells the (normalized) number of true detections we have. ROC curves facilitate the comparison between two or more detectors (in our case, filters): the curve that lies above in the plot is closer to the optimal performance than the curves below.

Fig. 8 shows the ROC curves for the different cases and channels under consideration. The solid line corresponds to the MF and the dashed line corresponds to the matrix filters. The number NT used for the plot is the total number of sources that are outside the masked area of the sky and that have fluxes above 150 mJy. The number FT is the total number of maxima found in the filtered images above the

minimum considered threshold. The plots are made for σ detection thresholds in the interval $\sigma \in [3, 10]$. For this range of detection thresholds, the ROC curve corresponding to the matrix filters is clearly above the one corresponding to the MFs for the 30, 44 and 70 GHz channels, meaning that if we fix any required spurious detection ratio we always have more true detections with the matrix filters than with the MFs. For the 100 GHz channels, the two curves run practically in parallel, but the MF is slightly above the matrix filters. This is related to the missing sources problem described in Section 4.2.2.

4.2.5 Flux estimation

Fig. 9 shows how both kinds of filters recover the fluxes of the sources in all the considered cases. Circles represent fluxes recovered with the MF and crosses represent fluxes recovered with the MTXF. There is an excellent agreement between true input and recovered fluxes for all the cases and between fluxes obtained with the MF and the MTXF. At low fluxes, the MF estimates show the well-known selection Eddington bias before than the MTXF. This is particularly evident at 44 and 70 GHz, but also visible at 30 GHz. As seen before, the MTXF-filtered maps have less noise than the maps filtered with the MF, and therefore the selection bias appears at a lower level. This also manifests in the smaller dispersion of crosses around the true value with respect to the circles. However, for very high fluxes it seems that MTXF tend to underestimate the flux of the sources. At 100 GHz, both filters lead to virtually the same results.

**Figure 8.** ROC curves for the filtering schemes and the four channels considered. Solid line: MF. Dot-dashed line: matrix filters.**Figure 9.** Estimation of the flux for the two filtering techniques. Circles: MF estimation. Crosses: matrix filter estimation.

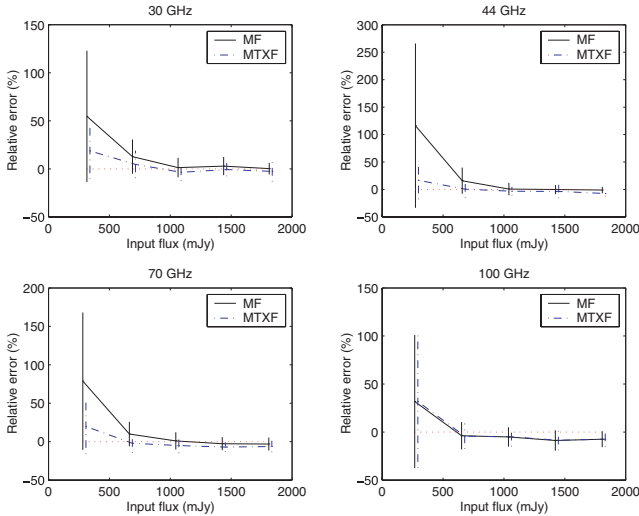


Figure 10. Relative flux estimation error and its dispersion. Solid lines: MFs. Dot-dashed lines: matrix filters. For clarity, the lines corresponding to the matrix filter have been slightly displaced towards the right.

Fig. 10 shows the relative flux error for the two filters and the four considered channels. We define the relative flux error as

$$e_{\text{rel}} = 100 \times \frac{\hat{S} - S_0}{S_0}, \quad (19)$$

where \hat{S} is the flux we estimate with the filters and S_0 is the input flux. We take five flux bins between the flux of the faintest detected source and 2 Jy, and for each bin we compute the average value and the dispersion of the relative error. The lowest bin is dominated by the Eddington bias. This bias can be quite large, as is the case for the MF at 44 GHz (115 per cent bias). The MTXF suffer less Eddington bias than the MF (except, as usual, for the 100 GHz case, where the two filters behave very similarly). As mentioned before, the dispersion around the mean value is smaller for the MTXF. Finally, it is worth noting the small negative bias suffered by both filters at high fluxes. This bias is not evident at 30 GHz, but it is easier to detect at higher frequencies. MTXF seem to be more biased (−6, −6 and −8 per cent at 44, 70 and 100 GHz, respectively, versus the MF biases that are −1, −3 and −8 per cent for the same frequencies). This kind of effect at high fluxes has been noted before in related filtering applications (Herranz et al. 2002b), and it is usually attributed to the non-ideality of the pixelized data that makes the process of calculation of the normalization of the filters imperfect. This normalization is obtained through equation (8), where the continuous analytical expression of the profiles τ_k (i.e. a Gaussian) is habitually used for the sake of velocity of computation, but in the real case the profiles take discrete values due to pixelization. This is the origin of a small mismatch that leads to the noticed small bias in the flux recovery, and it affects more channels with a smaller ratio between the beam FWHM and the pixel size (in this case, the 100 GHz channel). In any case, the bias is relatively small and can be calibrated by means of simulations or, alternatively, by using realistic discretized profiles, with a increased computational cost.

5 CONCLUSIONS

Although there is a relatively large number of works in the literature devoted to the detection of point sources in CMB images, there is practically no one that addresses the problem from the multifrequency point of view. The reason is that each individual EPS has

its own (a priori unknown) spectral behaviour and this makes it very hard to accommodate them in classic component separation schemes.

In this work, we apply a novel linear filtering technique, the ‘MTXF’, introduced by Herranz & Sanz (2008). MTXF incorporate full spatial information, including the cross-correlation among channels, without making any a priori assumption about the spectral behaviour of the sources. The basic underlying idea is that in all the considered channels the sources do appear in the same unknown positions (but with different, unknown intensities) and have known spatial profiles given by the experiment point spread function, while some components of the background (i.e. CMB and Galactic emission) are correlated among channels. Then a clever linear filtering/combination of images can lead to a substantial reduction of the background, and therefore to lower source detection thresholds. The resulting expression of the filters takes form of a matrix given in terms of the cross power spectra and the profile of the sources in the different maps.

We describe in detail the formalism of the MTXF, looking in detail into some particular cases of interest, and we apply them to the detection of radio sources in realistic all-sky *Planck* simulations at 30, 44, 70 and 100 GHz. In order to compare with a well-established single-frequency approach, we repeat the same process using the standard MF.

We compare both methods in terms of reliability, completeness, ROCs and flux accuracy. We find that for the three lower frequency channels (30, 44 and 70 GHz) the new MTXF clearly outperform the standard MFs for all these quality indicators. The MTXF significantly decrease the noise level, what translates into a lower detection threshold and a reduced number of false detections. The flux estimation is consequently improved, with a lower dispersion around the true input value and a lower flux at which the well-known selection Eddington bias occur. The improvement is particularly evident at 44 GHz. At 100 GHz, however, the performance of the two filters is very similar. We indicate some possible reasons for this behaviour, based on general analytical considerations about the structure of the filters.

One of the most interesting ways to compare two catalogues obtained with different methods is to set a fixed level of reliability, cut the catalogues at the corresponding points and compare how many detections there are in each of them. We find a notable increment of the number of true detections for a fixed reliability level obtained with the MTXF with respect to the standard MFs. In particular, for a 95 per cent reliability we practically double the number of detections at 30, 44 and 70 GHz: the ratio between the number of detections obtained with the MTXF and the MF for these channels are 1.8, 2.2 and 1.7, respectively.

We would like to stress once more on the importance of including multifrequency information in this approach. The new matched multifilters can be used to increase very significantly the number of EPS detections in upcoming CMB experiments such as *Planck* as well as in current experiments such as *WMAP*.

Although here we have tested the MTXF to the particular case of the detection of radio sources in the low frequency channels of *Planck*, the same technique can be easily applied to other frequency bands or to other fields of image analysis where point-like objects appear in different frames (images).

ACKNOWLEDGMENTS

The authors acknowledge partial financial support from the Spanish Ministry of Education (MEC) under project

ESP2004-07067-C03-01 and from the joint CNR–CSIC research project 2006-IT-0037. MLC acknowledges the Spanish MEC for a postdoctoral fellowship. JLS acknowledges partial financial support by the Spanish MEC and thanks the CNR ISTI in Pisa for their hospitality during his sabbatical leave. Partial financial support for this research has been provided to JGN by the Italian ASI (contracts Planck LFI Activity of Phase E2 and I/016/07/0 ‘COFIS’) and MUR. We acknowledge the use of the HEALPix (Górski et al. 2005) code for all sphere-based computations. The authors acknowledge the use of the PSM, developed by the Component Separation Working Group (WG2) of the *Planck* Collaboration. The simulations have been carried out using Grid infrastructure in the framework of the project EGEE (reference FP7 INFISO-R1 222667). The authors gratefully acknowledge the support obtained from this project.

REFERENCES

- Barreiro R. B., Sanz J. L., Herranz D., Martínez-González E., 2003, *MNRAS*, 342, 119
- Bennett C. L. et al., 2003, *ApJ*, 583, 1
- Carvalho P., Rocha G., Hobson M. P., 2008, preprint (arXiv e-prints, 802)
- Chen X., Wright E. L., 2008, *ApJ*, 681, 747
- Chiang L.-Y., Jørgensen H. E., Naselsky I. P., Naselsky P. D., Novikov I. D., Christensen P. R., 2002, *MNRAS*, 335, 1054
- de Zotti G., Toffolatti L., Argüeso F., Davies R. D., Mazzotta P., Partridge R. B., Smoot G. F., Vittorio N., 1999, in Maiani L., Melchiorri F., Vittorio N., eds, *AIP Conf. Ser. Vol. 476, The 3K Cosmology*. Planck Surveyor Mission: Astrophysical Prospects, American Institute of Physics, Woodbury, New York, p. 204
- de Zotti G., Ricci R., Mesa D., Silva L., Mazzotta P., Toffolatti L., González-Nuevo J., 2005, *A&A*, 431, 893
- Dickinson C., Davies R. D., Davis R. J., 2003, *MNRAS*, 341, 369
- Finkbeiner D. P., Davis M., Schlegel D. J., 1999, *ApJ*, 524, 867
- González-Nuevo J., Toffolatti L., Argüeso F., 2005, *ApJ*, 621, 1
- González-Nuevo J., Argüeso F., López-Caniego M., Toffolatti L., Sanz J. L., Vielva P., Herranz D., 2006, *MNRAS*, 369, 1603
- Górski K. M., Hivon E., Banday A. J., Wandelt B. D., Hansen F. K., Reinecke M., Bartelmann M., 2005, *ApJ*, 622, 759
- Haslam C. G. T., Salter C. J., Stoffel H., Wilson W. E., 1982, *A&AS*, 47, 1
- Herranz D., Sanz J. L., 2008, *IEEE J. Sel. Top. Signal Process.*, 2, 727
- Herranz D., Sanz J. L., Barreiro R. B., Martínez-González E., 2002b, *ApJ*, 580, 610
- Herranz D., Gallegos J., Sanz J. L., Martínez-González E., 2002c, *MNRAS*, 334, 533
- Hinshaw G. et al., 2007, *ApJS*, 170, 288
- Hobson M. P., McLachlan C., 2003, *MNRAS*, 338, 765
- Hobson M. P., Barreiro R. B., Toffolatti L., Lasenby A. N., Sanz J., Jones A. W., Bouchet F. R., 1999, *MNRAS*, 306, 232
- Kay S. M., 1998, *Fundamentals of Statistical Signal Processing, Volume 2: Detection Theory*. Prentice Hall PTR, Upper Saddle River, New Jersey
- Leach S. M. et al., 2008, *MNRAS*
- López-Caniego M., Herranz D., Barreiro R. B., Sanz J. L., 2004, in Bouman C. A., Miller E. L., eds, *Proc. SPIE, Vol. 5299, Computational Imaging II*. SPIE, Bellingham, p. 145
- López-Caniego M., Herranz D., Barreiro R. B., Sanz J. L., 2005b, *MNRAS*, 359, 993
- López-Caniego M., Herranz D., Sanz J. L., Barreiro R. B., 2005a, *EURASIP J. Appl. Signal Process.*, 15, 2426
- López-Caniego M., Herranz D., González-Nuevo J., Sanz J. L., Barreiro R. B., Vielva P., Argüeso F., Toffolatti L., 2006, *MNRAS*, 370, 2047
- López-Caniego M., González-Nuevo J., Herranz D., Massardi M., Sanz J. L., De Zotti G., Toffolatti L., Argüeso F., 2007, *ApJS*, 170, 108
- Naselsky P., Novikov D., Silk J., 2002, *MNRAS*, 335, 550
- Sanz J. L., Herranz D., Martínez-González E., 2001, *ApJ*, 552, 484
- Sanz J. L., Herranz D., López-Caniego M., Argüeso F., 2006, *Proc. European Signal Process. Conf. Vol. 14, Wavelets on the Sphere. Application to the detection problem*. EUSIPCO, p. 1
- Tauber J. A., 2005, in Lasenby A. N., Wilkinson A., eds, *Proc. IAU Symp. 201, New Cosmological Data and the Values of the Fundamental Parameters*. The Planck Mission. Astron. Soc. Pac., San Francisco, p. 86
- Tegmark M., de Oliveira-Costa A., 1998, *ApJ*, 500, L83
- The Planck Collaboration 2006, preprint (arXiv Astrophysics e-prints)
- Toffolatti L., Argüeso Gomez F., de Zotti G., Mazzei P., Franceschini A., Danese L., Burigana C., 1998, *MNRAS*, 297, 117
- Tucci M., Martínez-González E., Toffolatti L., González-Nuevo J., De Zotti G., 2004, *MNRAS*, 349, 1267
- Tucci M., Martínez-González E., Vielva P., Delabrouille J., 2005, *MNRAS*, 360, 935
- Vielva P., Barreiro R. B., Hobson M. P., Martínez-González E., Lasenby A. N., Sanz J. L., Toffolatti L., 2001, *MNRAS*, 328, 1
- Vielva P., Martínez-González E., Gallegos J. E., Toffolatti L., Sanz J. L., 2003, *MNRAS*, 344, 89
- Wright E. L. et al., 2008, preprint (arXiv e-prints, 803)

This paper has been typeset from a $\text{\TeX}/\text{\LaTeX}$ file prepared by the author.